Comparison of Radar and Video Observations of Shallow Water Breaking Waves

Merrick C. Haller and David R. Lyzenga

***Abstract*—Simultaneous microwave and video measurements of shallow water breaking waves are presented. A comparison of the data from the two sensors shows that short-duration spikes in the measured X-band radar cross section are highly correlated with the presence of breaking waves in the video imagery. In addition, the radar backscatter from shallow water breaking events is responsible for 40% to 50% of the total cross section, which is a much larger contribution than typically observed for deepwater breaking events. Based on estimates of the area of individual breaking regions determined from digitized video images, the radar cross section per unit area of the turbulent breaking region is shown to be well approximated by a value of −1.9 dB at 31° grazing. Finally, there are some differences between the radar and video signals that suggest that microwave radar may be less sensitive than video techniques to relict foam not associated with active wave breaking. In general, the results indicate that radar is a very good detector of shallow water breaking waves and suggest that radar can be used for the measurement of the spatial and temporal variations of wave breaking.**

***Index Terms*—Radar, sea spikes, surf zone, video remote sensing, wave breaking.**

I. Introduction

THE MEASUREMENT of the location and frequency of wave breaking events in shallow water is of significant interest because these events are the dominant forcing mechanism for several processes in the nearshore region. The breaking process transfers most of the energy and momentum associated with the organized wave motion into longshore currents [1], low-frequency gravity wave motions [2], and turbulence [3]. Additionally, the movement of sediment in the surf zone is closely related to these energy transfer processes and the beach topography is often encoded in the spatial variability of the mean locations of wave breaking (i.e., when averaged over time scales of 10–100 wave periods) [4].

Quantitative field measurements of individual wave breaking events are generally difficult, especially with *in situ* sensors. Various measurements have been tested with some success, such as sea surface elevations [5] and void fractions [6]. It is clear, however, that remote sensing techniques are the only feasible method for observing wave breaking over large spatial areas. To date, video recording is the most established remote sensing technique for detecting breaking waves (see [7], [8], and many others), but infrared [9], underwater sound [10], and microwave backscatter have also proven useful.

It has long been known that steep and/or breaking waves in the open ocean are associated with the presence of short-duration, large-amplitude bursts ("sea spikes") of radar backscatter (e.g., [11] and [12]) and that breaking waves appear as bright streaks in synthetic aperture radar (SAR) images [13]. SAR imagery from nearshore regions are often saturated with these streaks, which makes typical analysis of the surface wave field difficult or impossible. While wave breaking is clearly a dominant feature of nearshore areas, comparisons of simultaneous video and radar measurements have shown that sea spikes are not always caused by breaking wave events [14]–[16], and the exact relationship between wave characteristics and sea spikes remains unclear.

Most previous studies of radar backscatter have taken place in deep water, but recently there has been increased interest in using microwave radar as a tool for studying the nearshore environment. The few published applications of radar in the nearshore have suggested that radar measurements can be used to infer information on wave directional characteristics [17], bathymetry [18], [19], and wave energy fluxes [20]. However, since wave breaking is a primary source of radar scattering in these areas, it is necessary to better understand the influence of wave breaking on microwave returns in order to fully realize the potential for radar as a remote sensing tool in these areas. The following experimental study presents field measurements of microwave backscatter and simultaneous video from shallow water breaking waves. This type of data is rare in the literature, and this study offers a unique opportunity to assess the backscattered field from surf zone waves and to compare the breaking signatures observed by microwave and optical remote sensors.

II. Experiment

A. Description

These experimental data were collected during the multiinstitutional SHOWEX experiment conducted at the U.S. Army Corps of Engineers Field Research Facility (FRF) in Duck, NC in the fall of 1999. The microwave backscatter measurements were made with a coherent continuous-wave polarized scatterometer operating at X-band (10.5 GHz). The scatterometer was configured with two antennas, one for transmitting and receiving and one for receiving only. Signals from both antennas were mixed with the local oscillator signal so as to produce four output channels corresponding to the in-phase and quadrature

Manuscript received March 18, 2002; revised December 10, 2002. This work was supported by the Office of Naval Research (Littoral Remote Sensing Program) under the direction of F. Herr.

M. C. Haller is with the Department of Civil, Construction, and Environmental Engineering, Oregon State University, Corvallis, OR 97331 USA (e-mail: hallerm@engr.orst.edu).

D. R. Lyzenga is with the Ocean and Terrestrial Applications Group, Veridian Systems Division, Ann Arbor, MI 48109 USA (e-mail: david.lyzenga@veridian.com).

Digital Object Identifier 10.1109/TGRS.2003.810695

TABLE I
VIEWING PARAMETERS FOR PIER COLLECTION

graz. ang. (deg.)	look dir. (deg. T)	radar records	video records
31	104	2	0
31	124	5	5
41	104	1	1
46	124	1	1
46	134	1	1
46	144	1	1

signals for each antenna. However, the received signal from the transmit antenna suffered from excessive noise, so only data from the dedicated receive antenna are presented here (i.e., channels 3 and 4, in-phase and quadrature, respectively). Both antennas were vertically polarized for these data.

The scatterometer was mounted on the FRF pier with the antennas 9.4 m above the water surface, and a bore-sighted video camera was mounted on the scatterometer to record the optical signatures of breaking wave events. The 3-dB widths of the elliptical illuminated areas (footprints) of the radar were approximately 1.6 m $\times$ 2.4 m (31° grazing) and 1.1 m $\times$ 1.2 m (46° grazing) at range distances of 18.2 and 13.0 m, respectively. The footprints were small compared to the wavelength of the surf zone waves, and the turbulent breaking regions filled a considerable fraction of this footprint.

The grazing angles and look directions along with the number of data records for each run are listed in Table I. Each record was of approximately 5 min duration, and all were collected between 12 and 2 P.M. (EST) on November 5, 1999. Measurements of the wind–wave directional spectrum and ambient wind speed and direction are acquired year-round by the FRF. The wave spectra measured at the FRF offshore pressure sensor array during the pier collection are shown in Fig. 1. The incident wave field was dominated by narrow-banded swell arriving from the east (90° True). The significant wave height was 0.68 m, and the spectral peak frequency was 0.09 Hz. The winds were light at 3.9 m/s and from the southwest (206° True).

Bathymetric surveys are periodically conducted at the FRF site, and, fortunately, a survey was conducted on the day of the pier collection. The survey is shown in Fig. 2. The FRF pier is located at $y = 517$ m and is oriented along 72° T, and the radar footprint was always on the south side of the pier so that the angle between the radar look direction and the direction of wave approach ranged between 14° and 54°. It is clear from Fig. 2 that there is a depression under the pier. This localized depression, along with wave reflections from the pier pilings, tended to complicate the wave field close to the pier and led to significant differences between the illuminated wave fields at 31° and 46° grazing. This will be discussed further in Section III. Visual observations from the pier also indicated the presence of a moderate longshore current flowing to the north driven by the breaking of the obliquely incident waves.

B. Data Processing

Data runs lasted slightly less than 5 min; the output signals of all four data acquisition channels were sampled at $\sim$ 980 Hz, and bursts were written to disc at approximately 1-s intervals. The processing of the data involved corrections to account for nonideal amplifier gains and noise in the output signals due to internal instrument interference. The internal interference consisted of very short duration (typically 1–2 ms) negative voltage impulses in the raw signals, which were removed using a filter based on the instantaneous slope of the raw signal.

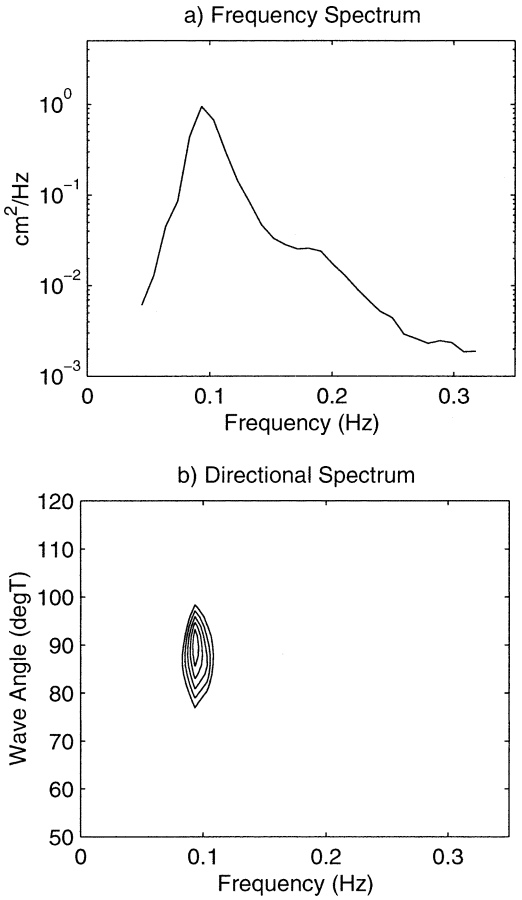

Fig. 1. (a) Frequency spectrum and (b) directional wave spectrum measured at the FRF offshore pressure sensor array (11/5/99, 1300 EST). Pier is oriented along 72° True.

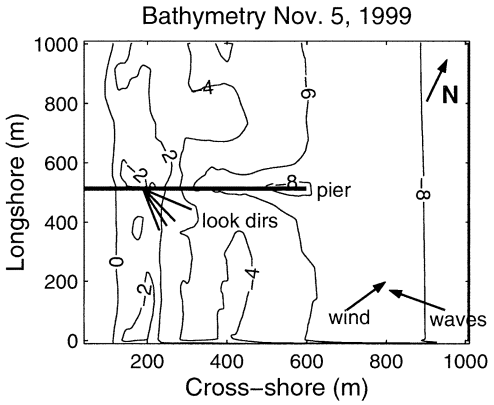

Fig. 2. Bathymetry contours from survey conducted on Nov. 5, 1999. Radar located on pier at cross- and longshore coordinates 177 and 517 m, respectively. Range distances to radar footprints are 18.2 and 13.0 m at grazing angles of 31° and 46°, respectively.

In order to calculate the time series of received power from each channel with high temporal resolution, each data run was divided into subintervals of 194 points. The received power (signal variance) for a given subinterval is then given by

$$p_n(t) = \frac{1}{193}\sum_{i=1}^{194}(r_i - \overline{r})^2 \tag{1}$$

where r_i is the recorded signal (proportional to the voltage at the output of the detector, after filtering); $\overline{r}$ is the signal mean; and n is the channel number. This resulted in a 1500-point time series of received power for each channel with each data point representing an averaging time of approximately 0.2 s.

The time series from each channel represent two independent measurements of the instantaneous backscattered power, and the ratio of the instantaneous powers from a given channel pair should be scattered about a constant equal to the effective channel gain ratio. However, during the data processing stage it was discovered that the raw signal was large enough to saturate the amplifier on the higher gain channel during the most energetic events.

The received power from both the in-phase and quadrature channel for all the subintervals from the entire data set analyzed herein are shown in Fig. 3. The plotted data indicate that when the received power is low the relationship between p_4 and p_3 is approximately linear. The linear fit to the low power points was calculated using all points where $p_4 < 2 \times 10^8$ counts^2 and is given by $p_4 = 7.185 \cdot p_3 - 1.707 \times 10^5$. The threshold on p_4 was essentially arbitrary, however, the linear fit compares very well with a linear fit to a smaller subset of points from intervals that did not contain any saturations. The nonzero intercept of the linear fit is due to the difference between the ratio of the background noise levels and the gain ratio.

Since the presence of the saturated points would cause the received power to be underestimated, an algorithm for estimating the amount of power lost due to saturations was developed. First, the entire set of recorded subintervals was fit to a third-order polynomial

$$p_4 = 1.322 \times 10^{-17} {p_3}^3 - 1.216 \cdot 10^{-8} \cdot {p_3}^2 + 4.274 \cdot p_3 + 1.283 \times 10^8$$

as shown in Fig. 3. Next, the power in channel four was shifted upwards by the amount equal to the vertical distance between the linear fit and the third-order curve, with those values calculated using the measured value of p_3. This correction was applied to all data where $p_4 > 2.749 \times 10^8$, which is the intersection point of the two curves. Absolute calibration was achieved by recording the signals from a known reflector (a 6-in aluminum sphere) placed at a series of locations within the antenna beam. The calibration procedure established a relationship between the received power and the radar cross section σ. The calibration measurements were also used to confirm the theoretical antenna gain pattern, $G(\theta, \phi)$, for the horn antennas. The antenna gain pattern was then used to determine the illuminated area, which is defined as

$$A = \int\int G(\theta, \phi) dx dy \tag{2}$$

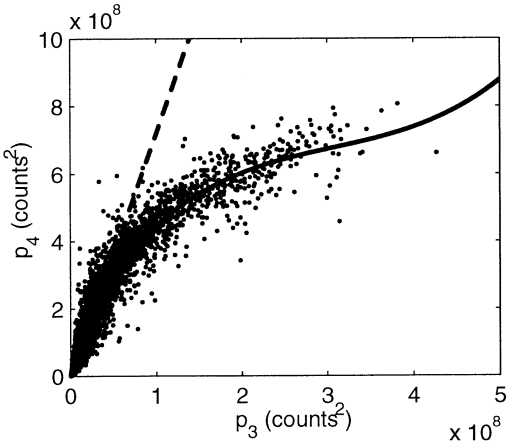

Fig. 3. Received power in channel four versus received power in channel three for all data runs from the pier. The linear fit to the low power points is shown as the dashed line. The fit to the high power data points is shown as the solid line.

where x and y are the horizontal coordinates at the surface, and θ and ϕ are angular coordinates that are related to x and y by simple geometric considerations. Having determined the radar cross section and illuminated area, we then define the normalized radar cross section, or radar cross section per unit area as $\sigma^0 = \sigma/A$. Based on the agreement between the calibration measurements and the theoretical antenna pattern, we estimate the calibration accuracy to be better than 1 dB.

The correction procedure for signal saturations was employed in order to improve the accuracy of the measurements of instantaneous backscattered power. This correction procedure is made possible by the fact that the two channels of data provide a redundant estimate of backscattered power. However, it should be noted that the correction procedure essentially reduces the degrees of freedom in the calculation of net backscattered power and, therefore, increases the effect of sampling variability and noise.

III. Breaking-Wave Detection

The association of wave breaking with sea spikes has been known for several decades, yet relatively few quantitative comparisons between radar backscatter and optical signatures of wave breaking have been made. Lewis and Olin [21] appear to be the first to attempt such a comparison and their study is also the only one to consider shallow water breaking waves. Jessup *et al.* [14] presented observations of sea spikes and found that 70% of the sea spikes observed using a Ku-band (14 GHz) radar operating at 45° grazing were associated with whitecaps recorded by a bore-sighted video camera. Though sea spikes have been observed at all grazing angles [22], they are more prominent above the ambient (nonbreaking) background signal in low grazing angle (LGA) measurements. Liu *et al.* [15] found that only approximately 30% of the observed sea spike events were associated with deepwater whitecaps for LGA measurements (angles less 20°), while the remainder were attributed to "steep" wave features. However, whitecaps accounted for a much larger percentage of the total backscattered power, which indicates their importance to the overall returns. In a related

work, Frasier *et al.* [16] found that a large range of whitecap coverages mapped to a comparably smaller range of sea spike coverages. Thus, they concluded that sea spike coverage has a significant dependence on ocean surface features that do not yield an optical signature.

Nonetheless, at intermediate grazing angles sea spikes are better correlated with active wave breaking. Obviously, any technique for measuring wave breaking is dependent to some extent on the definition of what constitutes a wave breaking signature, whether it is based on video intensity, backscattered power, or any other measurable quantity. Jessup *et al.* [14] found the best correspondence between the microwave and optical breaking signatures when the sea spikes were defined by a combination of Doppler bandwidth exceeding 50 Hz and normalized radar cross section (NRCS) values over -6 dB. However, they did not strictly require the whitecaps observed in the video to occur within the 3-dB radar footprint. Whitecaps that occurred up to 5 m downwave of the footprint were also counted. This, in effect, allowed some steep incipient breakers to be counted as breaking waves. They also restricted their analysis to whitecaps with lengths greater than 0.5 m in the propagation direction. Finally, it should be noted that none of these previous studies have analyzed the measured optical intensity signal; instead, wave breaking was determined based on somewhat subjective visual estimates.

The reason for the varying degrees of correlation between sea spikes and breaking waves is likely related to the relative importance of specific scattering mechanisms as a function of grazing angle. A number of potential scattering mechanisms from steep and/or breaking waves have been described in the literature. The mechanisms likely to be of highest importance at intermediate grazing angles are quasi-specular scattering from the forward faces of steep breaking or near-breaking waves [23], [14], edge diffraction from sharply peaked wave crests [24]–[26], and Bragg scattering from the increased surface roughness generated during the breaking process [23], [27].

The field measurements of Jessup *et al.* [14] showed the maximum NRCS occurred upwave of the crest at the location of maximum surface slope; hence, those authors had attributed the majority of their observed sea spikes to specular scattering. In addition, those authors found no significant correlation between whitecap size and the measured microwave parameters. However, their video analysis was only qualitative in nature. Walker *et al.* [28] collected laboratory measurements of stationary breaking waves with an X-band radar operating at 45° grazing. Their data showed that the maximum NRCS occurred near the turbulent region at the wave crest, which is also a region of high surface roughness, and suggested a Bragg-like mechanism similar to that proposed by [27].

Here we perform a quantitative comparison between the microwave parameters and the measured intensity variations recorded by the video camera, and we show that the measured sea spikes are highly correlated with the presence of breaking waves in the video images and that the total backscattered power is proportional to the size of the imaged turbulent breaking region, which suggests that the dominant backscatter source is the highly roughened surface of the breaking region.

A. Radar Sea Spikes

In order to analyze the relationship between sea spikes observed at intermediate grazing angles and shallow water breaking waves, a sea spike definition must be adopted. Here we define a sea spike as simply any excursion above the mean NRCS containing more than one data point (i.e., duration > 0.2 s). This definition is chosen instead of the absolute NRCS threshold of -6 dB used by Jessup *et al.* [14] for several reasons. First, their definition was based on measurements from only one grazing angle and it is presently unknown how the NRCS from active breaking regions depends on grazing angle. Second, an absolute power threshold is subject to calibration uncertainties between radar systems. Third, the previous criteria were developed for wave breaking in the open sea, which is very different from shallow water breaking induced by interaction with the sea bottom. So, in light of these three factors, the present definition is chosen for its simplicity.

Lewis and Olin [21] were the first to consider the scattering from the highly roughened surface of whitecaps. They hypothesized that whitecaps behave as isotropic reflectors, and that their NRCS should be approximately 3 dB. Their LGA measurements indicated that when a whitecap approximately filled a resolution cell the sea spike amplitude approached 1.8 dB, which loosely confirmed their hypothesis. Phillips [29] formally defined the NRCS as the sum of two separate contributions

$$\sigma^0 = \sigma^0_B + \sigma^0_{\rm ss} \tag{3}$$

where σ^0_B is the Bragg contribution, and $\sigma^0_{\rm ss}$ is the sea spike contribution from localized breaking wave sources. Phillips assumed $\sigma^0_{\rm ss}$ would have a functional dependence on grazing and look direction relative to the wind, and would increase at low grazing angles and be a maximum for upwind looks.

Here we adopt the following notation: the measured NRCS time series is considered a summation of contributions from the sea spikes and the ambient background given by

$$\sigma^0(t) = \sigma^0_{\rm ss}(t) + \sigma^0_a(t) \tag{4}$$

and the time-averaged mean NRCS for an individual record is

$$\overline{\sigma^0} = \frac{1}{T}\int_0^T \sigma^0(t)dt \tag{5}$$

where T is the record duration ($T \approx 300$ s for these data), and

$$\sigma^0_{\rm ss} = \begin{cases} 0 & \sigma^0 < \overline{\sigma^0} \\ \sigma^0(t) & \sigma^0 > \overline{\sigma^0} \end{cases} \tag{6}$$

$$\sigma^0_a = \begin{cases} \sigma^0(t) & \sigma^0 < \overline{\sigma^0} \\ 0 & \sigma^0 > \overline{\sigma^0}. \end{cases} \tag{7}$$

Fig. 4(a) and (b) shows time series of NRCS collected at both 31° and 46° grazing along with the mean NRCS used as the threshold for defining sea spikes. Frequent sea spikes are clearly evident and distinct from the low-level ambient background signal. For these data, the sea spikes are more frequent and are larger in amplitude at higher grazing angles.

There were a total of 50 min of simultaneous video and radar measurements, encompassing a range of grazing angles and

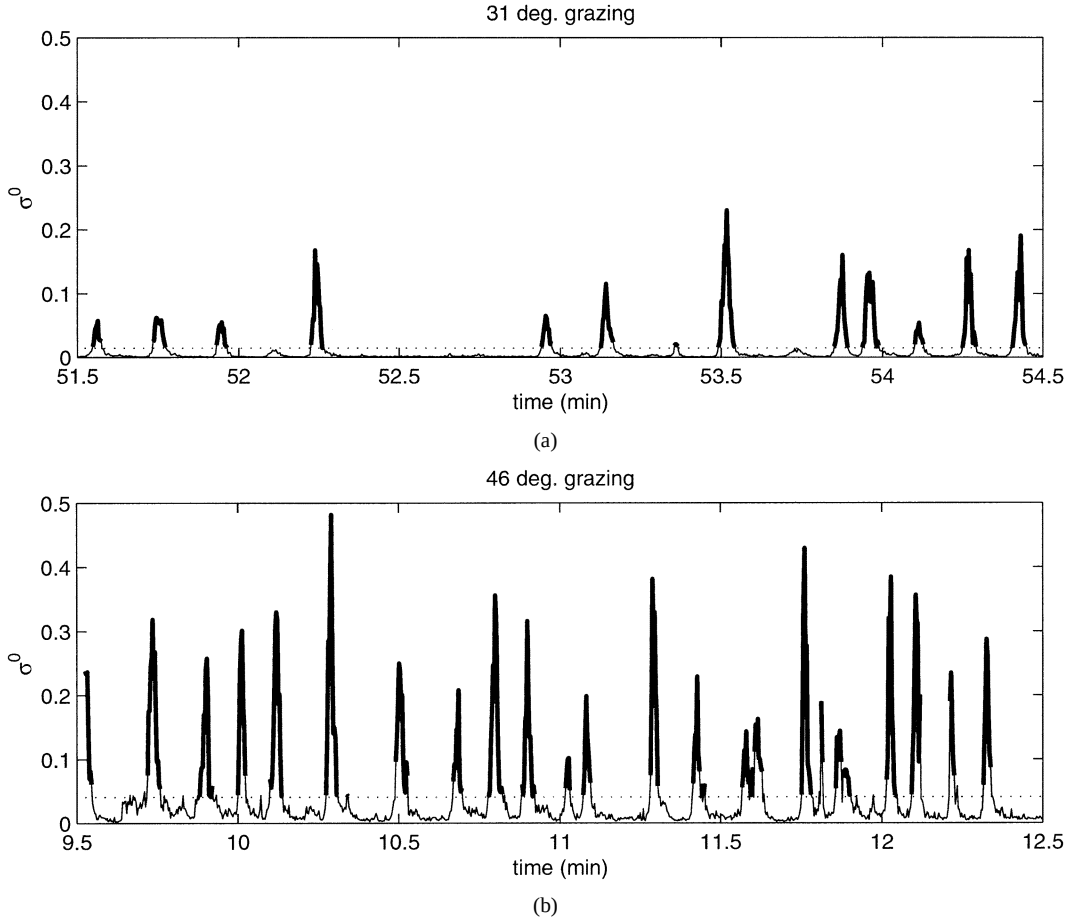

Fig. 4. Time series of NRCS at (a) 31° and (b) 46° grazing. Sea spikes are defined as excursions above $\overline{\sigma^0}$ (dotted line) and are shown as thick lines.

look directions. Based on the radar calibration data the 3-dB radar footprint was demarcated as a red ellipse on the digitized video images during post processing. An initial comparison between the video records and the NRCS time series showed that for the 306 sea spikes observed in the radar data, 92% of the spikes were associated with some degree of visual wave breaking. There was no restriction placed on the observed size of the breaking event, but only events that clearly occurred within the 3-dB footprint were counted. The comparison of the radar measurements with the video suggests that the observed sea spikes serve as a good detector of shallow water breaking events.

Since the water depth of the illuminated area was shallow ($\sim$ 1.5 m) and the incident wave spectrum was narrow-banded, most of the wave crests passing through the footprint were breaking. However, the location of the footprint was dependent on grazing angle with the footprint being closer to shore and the pier at larger grazing angles. At 41° and 46° grazing the increase in sea spike frequency was due mainly to the reflection of waves from the pier, although other factors may also have been present. Some of the reflected waves appeared to break due to their interactions with the longshore current, which was flowing northward toward the pier. These small breakers also generated sea spikes. Therefore, in some respects the wave conditions were very different between the 31° and 46° data runs. For the higher grazing angle cases the direction of breaking wave propagation with respect to the look direction was highly variable, the along-crest nonuniformity of the wave crests was increased, and the underlying causes of wave breaking were different from standard shoaling effects. Since, for example, the radar cross section of breaking waves is expected to vary significantly with look direction, the highly variable wave field close to the pier has significantly limited our ability to make a straightforward comparison between grazing angles as will be discussed further in a later section.

A small number of incipient breakers or highly steepened unbroken waves also occurred during observations at all grazing angles. However, for these data the comparison with video indicates that the sea spike criterion does a very good job of sorting out the steep waves from the breaking waves, and the dependence of sea spike frequency on grazing angle is directly related to the environmental effects that led to increased breaking frequency.

The average sea spike amplitude is given by

$$\text{mean}\,[\sigma^0_{\text{ss,max}}] = \frac{1}{N}\sum_{i=1}^{N}\sigma^0_{\text{ss,max}}(i) \tag{8}$$

where $\sigma^0_{\text{ss,max}}(i)$ are the set of individual spike maxima for a given record containing N sea spikes. Fig. 5 shows the variation of the average spike amplitude versus grazing angle and look direction. The figure indicates that there is some dependence of sea spike amplitude on grazing angle. However, there is no

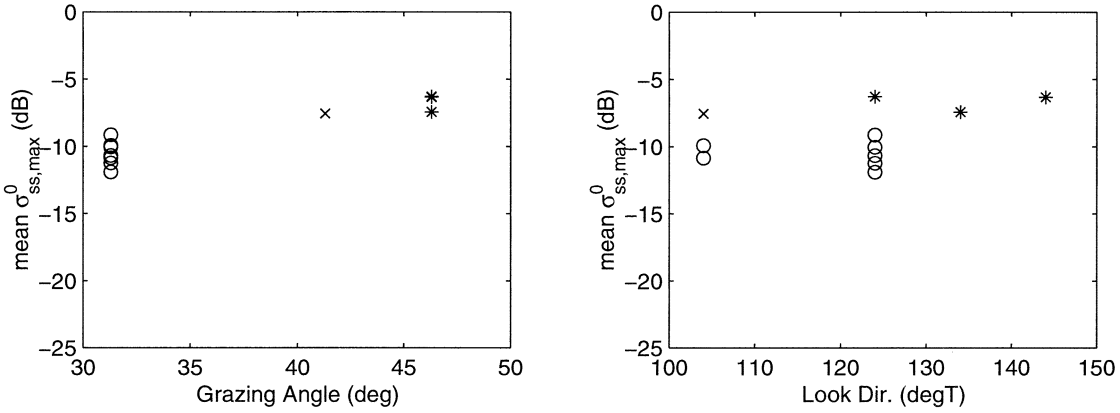

(a) (b)

Fig. 5. Variation of average sea spike amplitude with (a) grazing angle and (b) look direction. Symbols correspond to grazing angle.

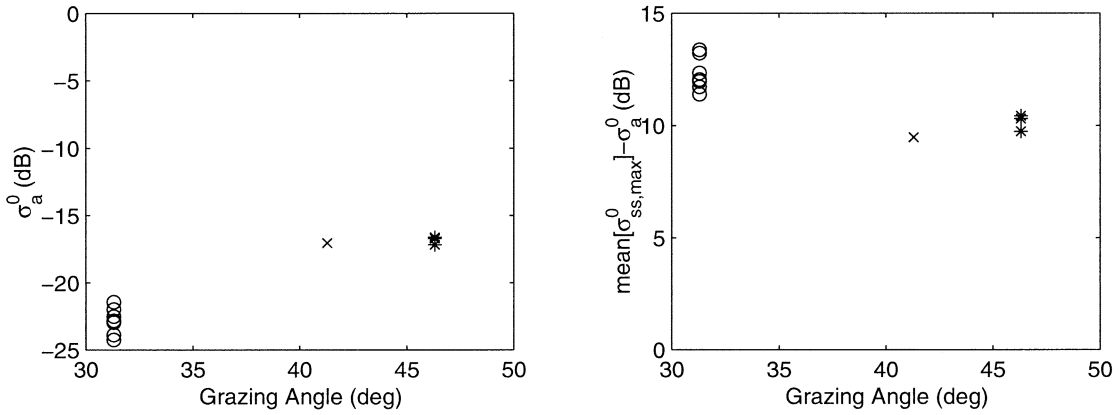

(a) (b)

Fig. 6. Variation of (a) ambient signal ($\overline{\sigma^0_a}$) with grazing angle, (b) sea spike contrast over ambient signal with grazing angle. Symbols correspond to grazing angle.

systematic dependence on the look direction with respect to the waves for the range of angles considered here.

Fig. 6(a) shows the variation of the time-averaged ambient signal ($\overline{\sigma_a}$) with grazing angle. The ambient signal shows a significant increase with grazing angle, which is expected based on traditional models of two-scale Bragg scattering from nonbreaking waves. The detectability of breaking waves is directly related to the contrast between the individual spikes and the ambient background signal, which is shown in Fig. 6(b). It is evident that the ambient signal increases faster with grazing angle than the sea spike signal indicating that at lower grazing angles the sea spikes are more clearly visible above the ambient background. Nonetheless, even at 46° grazing, the sea spikes are $\sim$ 10 dB higher than the ambient signal. Also, sea spikes appear to be much more important in the surf zone than in deep water. The contribution of the sea spikes to the total cross section is approximately 40% to 50% for these data, as opposed to the 5% to 15% contribution found in deep water (vertical–vertical polarization) by Jessup *et al.* [30]. Much of this observed increase can be attributed to the higher probability of wave breaking in the surf zone. However, the net contribution of individual sea spikes (sea spike cross section integrated over the sea spike duration) is also somewhat higher for shallow water versus deep-water breakers ($-$35 dB versus $-$43 dB; see [31, Fig. 6(a)]).

B. Radar/Video Comparison

The bore-sighted video camera was operated simultaneously with the radar and recorded black and white movies of the sea surface. The radar and video recordings were synchronized at the beginning of the pier collection using a time code generator. The time code generator stamped each video frame with the current time while the radar queried the time code generator at the beginning and end of each burst sample. During postprocessing, the movies were downsampled to a rate of 5 Hz and digitized using video capture image processing software on a standard PC. This allowed us to make quantitative comparisons between the gray scale intensity of the video images and the measured radar backscatter.

Fig. 7 shows three video frames taken at 31° grazing. The superimposed ellipses near the centers of the images mark the perimeter of the 3-dB angular beam width. The solid shading at the left-hand side of the frames is due to one of the antennas being in the field of view. The superimposed parallel transects are approximately oriented in the direction of wave propagation and traverse the wave profile at two separate locations along the wave crest. The pixel intensities along the transects are shown in the right-hand panels. Since the breaking region was expanding in the along-crest direction, the transects are

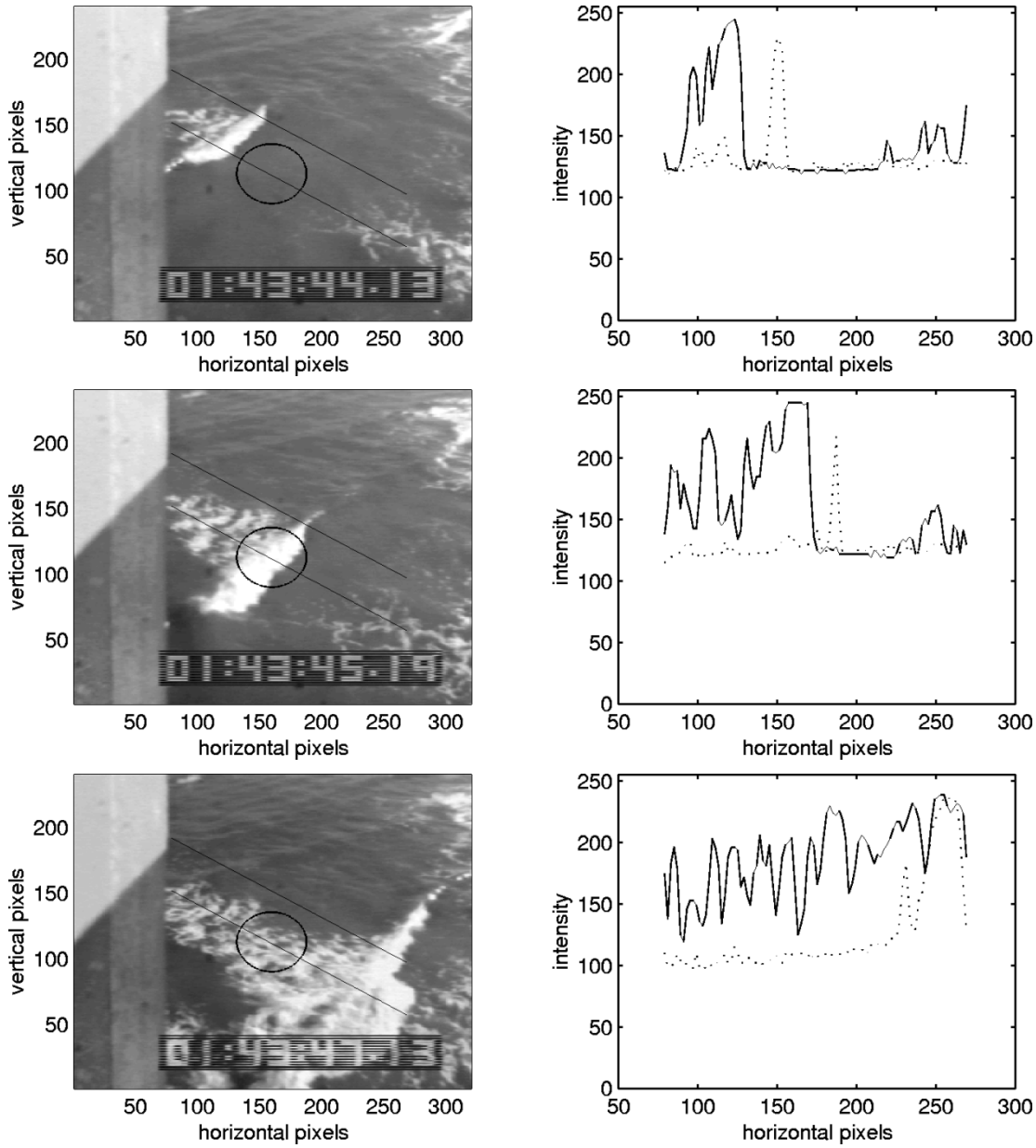

Fig. 7. (Left) Video frames from a data record at 31° grazing and 124° T look direction. (Right) Pixel intensities for the linear transects shown in video frames (lower transect: solid line, upper transect: dotted). Grayscale intensity varies between 0 (black) and 255 (white). Timestamp in video images has units hrs:min:sec.sec/30 EST.

located at different stages in the breaking process. In all three images the leading edge of the breaking region is well defined as a sharp increase in intensity in the upwave direction. The upper transects cross the wave profile at earlier stages in the breaking process and the active breaking region appears as an isolated intensity spike above a nearly constant darker background. As the wave propagates through the scene, the upper transects show a widening of the intensity spike and it begins to develop a second spike on its trailing edge. These trailing regions of higher intensity are the result of relict turbulence and/or foam being shed from the wave crest and left behind. The lower transect crosses the wave at a later stage of breaking and shows numerous trailing spiky features of gradually weakening intensity. This trailing foam is visible as a splotchy area in the video frame and often remains stationary on the water surface for many seconds before dissipating. In fact, the rightmost edge of the lower transect shows a region of relict foam left from a previous breaker that remains stationary as the breaker moves through the scene toward it.

The results discussed in Section III-A suggest that radar sea spikes are well correlated, at least qualitatively, with optical (whitewater) signatures of breaking waves and that radar backscatter from the active breaking regions is much greater than from other parts of the water surface. To examine this relationship more quantitatively, we used the video imagery to delineate breaking regions by means of a threshold on the image intensity. The procedure for doing this is described in further detail below, but, in essence, we assigned a value (a_{ij}) to each pixel according to whether it was breaking ($a_{ij} = 1$) or nonbreaking ($a_{ij} = 0$) where i and j are indices that indicate

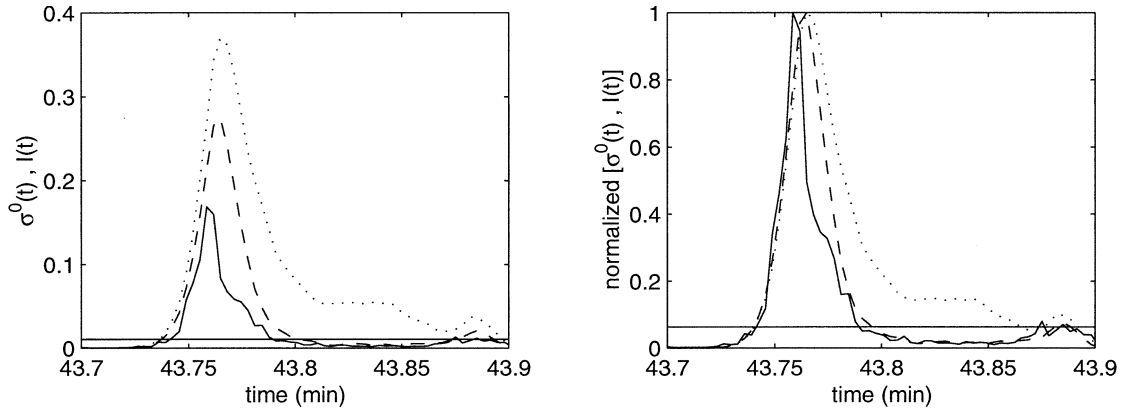

(a) (b)

Fig. 8. (a) Portion of the σ^0 time series (solid) for the breaking event shown in Fig. 7 with corresponding $I(t)$ calculated using intensity thresholds 225 (dashed) and 205 (dotted) (b) same as (a) except the records are normalized by their local maximum. Horizontal line is the mean of σ^0 used to define sea spikes. The highest correlation between σ^0 and $I(t)$ occurs at threshold 225 (see Fig. 10).

the position within the image. We then define a beam-filling factor

$$I = \sum_i \sum_j \frac{a_{ij} G_{ij} \Delta x \Delta y}{A} \tag{9}$$

where G_{ij} is the antenna gain at a given pixel location; Δx and Δy are the pixel dimensions; and A is the illuminated area defined in Section II. Thus, $I = 0$ if there are no breaking regions within the illuminated area, and $I = 1$ if the illuminated area is completely covered by breaking water. We also refer to the numerator in this expression as the breaking area A_b. In particular, we investigated the hypothesis that the total radar cross section σ is proportional to A_b, or equivalently that the normalized radar cross section $\sigma^0 = \sigma/A$ is proportional to I. The constant of proportionality in either case is denoted by σ_b^0 and may be interpreted as the radar cross section per unit breaking area. We also investigated the dependence of this parameter on grazing angle.

Defining wave breaking and, therefore, estimating A_b in video images has its difficulties. For example, as seen in Fig. 7, while an absolute intensity threshold may be applied to the upper transects to define the breaking region, a similar threshold applied to the lower transect is likely to include relict foam in the estimated breaking region. In addition, it is unclear how comparisons can be made between different viewing geometries, since pixel intensity is a relative measure dependent on the ambient light conditions and the camera aperture. However, at this stage imposing an intensity threshold seems to be the simplest first approach and is consistent with the method used to define sea spikes. Therefore we define a threshold video intensity whereby the brightest regions of the image are isolated and denoted as active breaking regions. The procedure for determining I is to scan the 3-dB footprint in each video frame for intensity values exceeding the threshold and then create a binary mask of ones and zeros where the ones are the locations of pixels exceeding the threshold (we do not require the mask to be contiguous). This mask demarcates A_b for a given image and the beam-filling factor I can then be calculated from (9).

Fig. 8(a) shows a sea spike and the corresponding beam-filling factor based on two different thresholds for the wave breaking event shown in Fig. 7. It is evident from the figure that the sea spike occurs simultaneously with the beam-filling spike, and that spikes from both sensors are fairly similar in shape. However, lowering the intensity threshold clearly increases I, especially near the maxima and along the trailing edges. The similarity of the sea spike and the beam-filling spike strongly suggests a correlation between the NRCS and the size of the breaking region within the footprint. In fact, the three video frames shown in Fig. 7 correspond to the initiation of the sea spike (i.e.,σ^0 rises above $\overline{\sigma^0}$), the sea spike maximum, and the conclusion of the sea spike event. Comparison of the time axis shown in Fig. 8(a) with the timestamps on the video frames shows that the sea spike is initiated an instant before the breaking wave enters the footprint, reaches its maximum amplitude when the breaker is at bore center, and ceases shortly after the crest has exited the footprint. However, the differences between the beam-filling spikes for each intensity threshold suggest that the magnitude of I and the shape of the trailing edges of beam-filling spikes are highly dependent on the chosen threshold.

Fig. 8(b) shows the same data as Fig. 8(a), except the sea spikes and the beam-filling spikes are each normalized by their local maxima in order to better examine the absolute spike shape. The normalized spikes indicate that the shapes of both can be remarkably similar if the proper intensity threshold is chosen; however, the threshold cannot be known *a priori*. This indicates that the higher tails of the beam-filling spikes, which are caused by the trailing foam, can be significantly reduced by the choice of intensity threshold. However, even the sea spike shows some front-to-back asymmetry, which suggests that the area of surface roughness that causes increased radar scattering spreads out on the trailing edge of the breaking crest. Yet, the sea spike still appears to have a somewhat narrower peak compared to the beam-filling spike suggesting that the breaker inherently has trailing whitewater that is not associated with surface roughness and active breaking, and therefore does not lead to radar scattering. This trailing foam of lower surface roughness also causes the beam-filling maxima to occur after

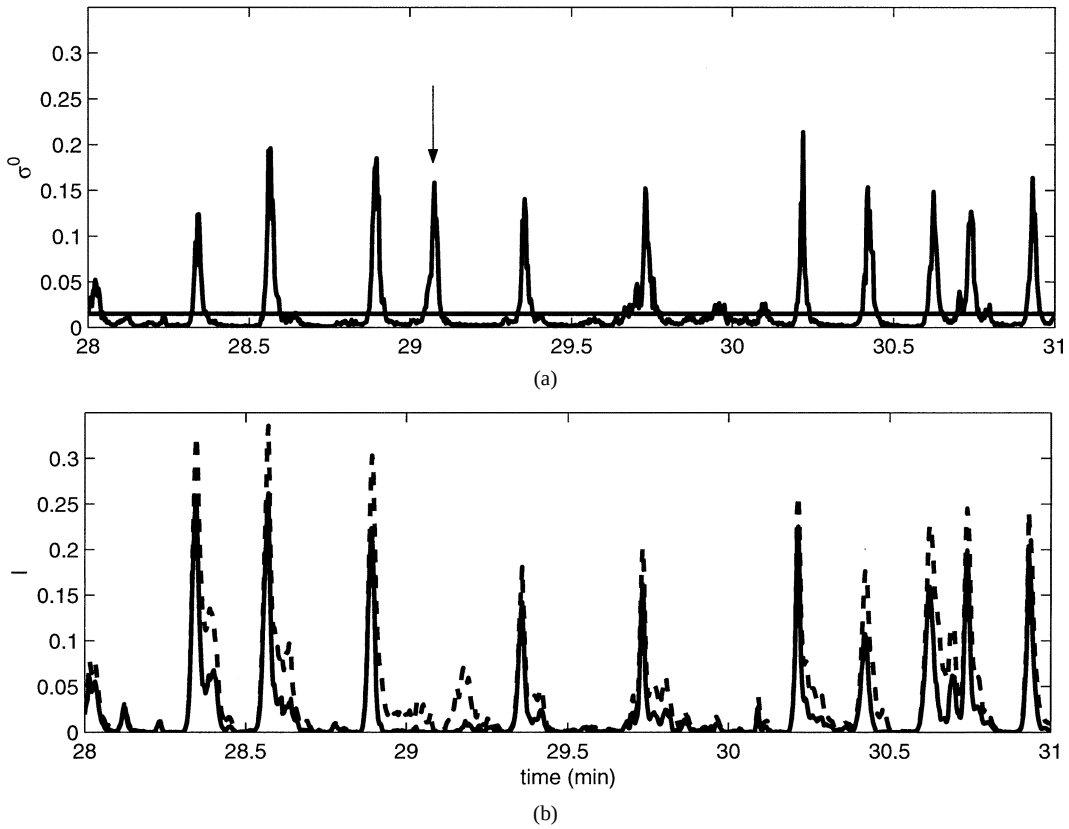

Fig. 9. (a) σ^0 at 31° grazing. (b) Corresponding beam-filling factor at threshold 215 (solid) and 205 (dash-dot).

the sea spike maxima (which occurs when the crest is at bore center). Instead, the beam-filling maxima occur approximately when the crest has completely traversed the footprint and the footprint is nearly filled with whitewater. This is an important difference since examination of the video in playback mode shows that the area of whitewater that is observed to propagate with the wave crest is smaller than the footprint, and therefore the "true" breaking area would peak when this narrow breaking region at the crest is at bore center.

Fig. 9 shows a larger portion of σ^0 and I time series (using two different intensity thresholds) from another data record at 31° grazing and look direction of 124° True. It is evident that for both thresholds the beam-filling factor shows numerous spiky fluctuations similar to σ^0. It should be noted that σ^0 and I were not sampled exactly simultaneously; therefore, I was resampled using linear interpolation to match the sample times of σ^0. This interpolation made only minor differences and does not change the nature of the results.

Although Fig. 9 shows that σ^0 and I appear to be very well correlated over the entire record, there are some differences. For example, just after $t = 29$ min there is a sea spike that does not have a corresponding increase in the breaking area. Examination of the video playback shows that this sea spike occurs simultaneously with a breaking wave, but this wave had been breaking for several meters before it entered the footprint. As the breaking proceeded the whitewater became well mixed and splotchy. Therefore, the breaking region passed below the video intensity threshold and did not generate a spike in I. Nonetheless, the increased surface roughness of the breaker generated a sea spike. Occasionally for some runs, especially at the higher grazing angles, relict foam on the water surface was advected through the video frame and generated beam-filling spikes when no breaking waves were present (and there was no corresponding sea spike). These mismatches between the sea spikes and beam-filling spikes were not common, but they do indicate that the two sensors are measuring different quantities, i.e., the video intensity is sensitive to air entrainment while the radar backscatter is sensitive to surface roughness.

C. NRCS of Breaking Waves

Quantitative estimates of the NRCS for areas of active breaking (σ_b^0) can be made based on the constant of proportionality between $\sigma_{\rm ss}^0$ and I. However, in order to make these comparisons using multiple records, a systematic method for choosing the video intensity threshold is needed. Therefore, for this analysis each video record was processed for a range of thresholds and the correlation coefficient (r^2) between σ^0 and I was calculated. The variation of the correlation coefficient with intensity threshold for each record is shown in Fig. 10. For the 31° runs the beam-filling factor is generally well correlated with the NRCS for a range of thresholds and the correlations tend to increase for more restrictive thresholds, since the higher thresholds remove the relict foam and decrease the tails of the I spikes. The correlation coefficients are highest when both the number and shape of the spikes recorded by the two sensors closely correspond. If the threshold becomes too restrictive, breaking waves do not generate spikes in I and correlations quickly decrease.

Fig. 10(b) shows the influence of the intensity threshold on the correlations at higher grazing angles. The data run at 41°

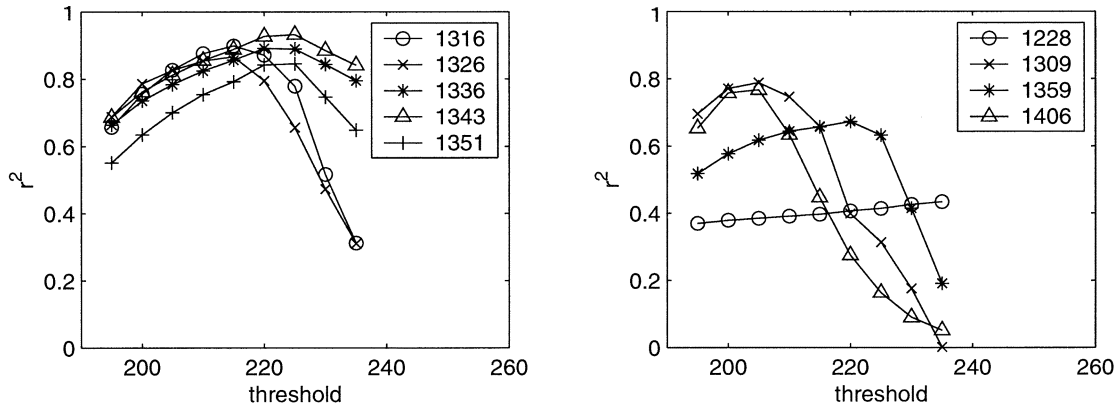

(a) (b)

Fig. 10. Correlation coefficient between σ^0 and I as a function of video intensity threshold for (a) 31° grazing and (b) 41° (1228 EST) and 46° grazing. Run start times are given in EST (see also Table I).

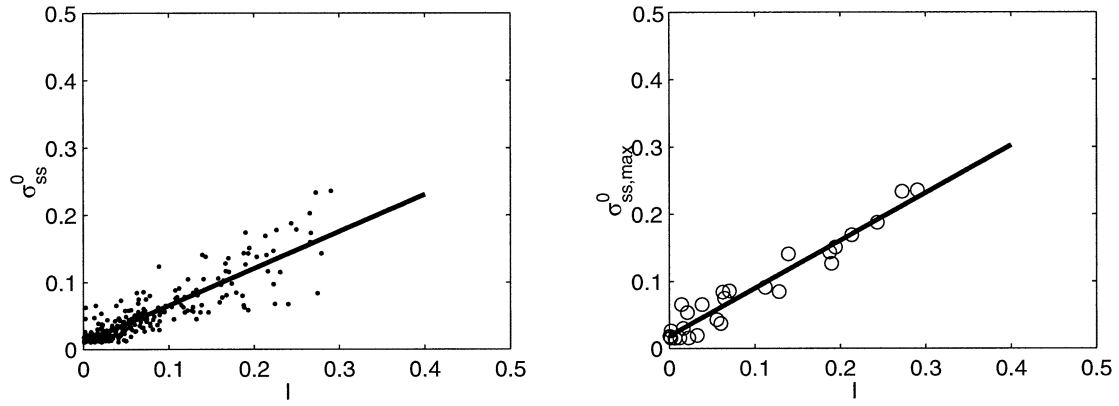

(a) (b)

Fig. 11. Instantaneous $\sigma^0_{\rm ss}$ versus I during (a) sea spike events (slope $= 0.55$, $r^2 = 0.88$) and (b) only at sea spike maxima (slope $= 0.71$, $r^2 = 0.97$). Data includes all spike events observed in the data record from which Fig. 7 was derived, with video intensity threshold of 225.

does not show a well defined correlation maximum. This was primarily a result of poor contrast between the broken and unbroken water surface in the video images due to the ambient light conditions and the aperture settings on the camera. No effort was made to postprocess the video images to improve the contrast and the video data from this run were not used further. The correlations at 46° are generally lower than those found at 31°. This is because the wave field was much more choppy with smaller more dispersed breaking events traveling in wide range of directions due to the effects of the pier, as discussed previously. There was also more relict foam on the water surface near the pier and this reduced contrast between the broken and unbroken water surface.

Choosing the intensity threshold that gives the highest correlation with the NRCS allowed us to optimize the binary mask to overcome the inherent ambiguity between active breaking and foam in the video recording process. Visual inspection of the binary mask images further indicated that the areas demarcated by the mask were reasonable estimates of areas of active wave breaking. Optimizing the binary mask also accounted for variations in the ambient light. For example, the five records used in Fig. 10(a) were obtained with the same viewing geometry during the middle of the day (1315 EST to 1356 EST) and the threshold of maximum correlation shifts during this period from 215 to 225; possibly the result of a steady increase in the ambient light.

If we focus our attention on a "clean" video record, wherein the breaking waves tended to approach at a constant angle to the radar and relict foam patches were not advected through the video images, we can make a straightforward estimate of σ^0_b. Fig. 11(a) directly compares the instantaneous values of $\sigma^0_{\rm ss}$ and I for all the sea spike events contained in the data record from which Fig. 7 is derived. The data are highly correlated ($r^2 = 0.88$) and strongly suggest a linear relationship between the measured NRCS and the beam-filling factor calculated from the video. A linear fit to the data was calculated using a least squares method and the NRCS of the breaking region given by the slope of this line is $\sigma^0_b = 0.55$ (-2.6 dB). The scatter of points below the linear fit to the data likely occur after the breaker has passed by bore center, when the beam-filling spikes exhibit their higher amplitude tails. Since the sea spike maxima occur when the breaker is at bore center, comparing only the instantaneous values at the sea spike maxima will tend to reduce the effect of the trailing foam. The subset of this data corresponding to the sea spike maxima are shown in Fig. 11(b), and indeed, the NRCS maxima are highly correlated ($r^2 = 0.97$)

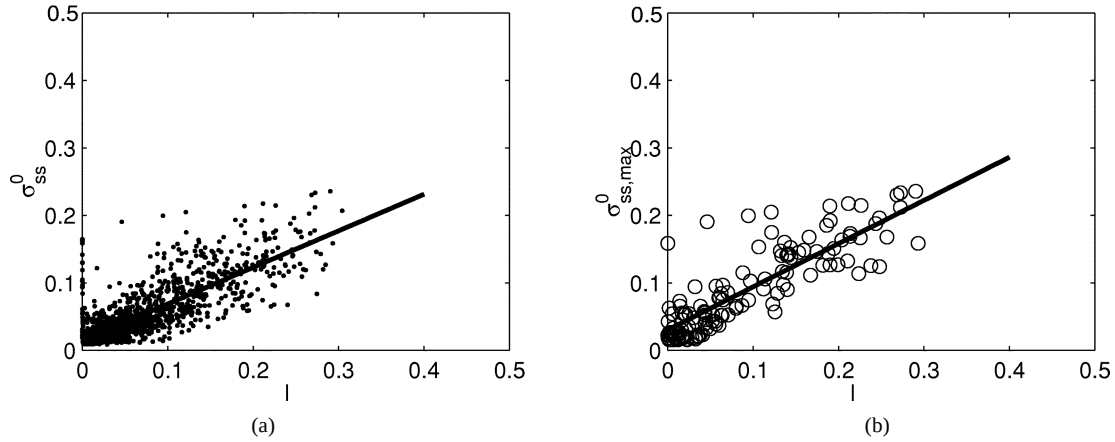

Fig. 12. Instantaneous σ^0_{ss} versus I during (a) sea spike events (slope $= 0.54$, $r^2 = 0.82$) and (b) only at sea spike maxima (slope $= 0.64$, $r^2 = 0.87$), using all video data at 31° grazing.

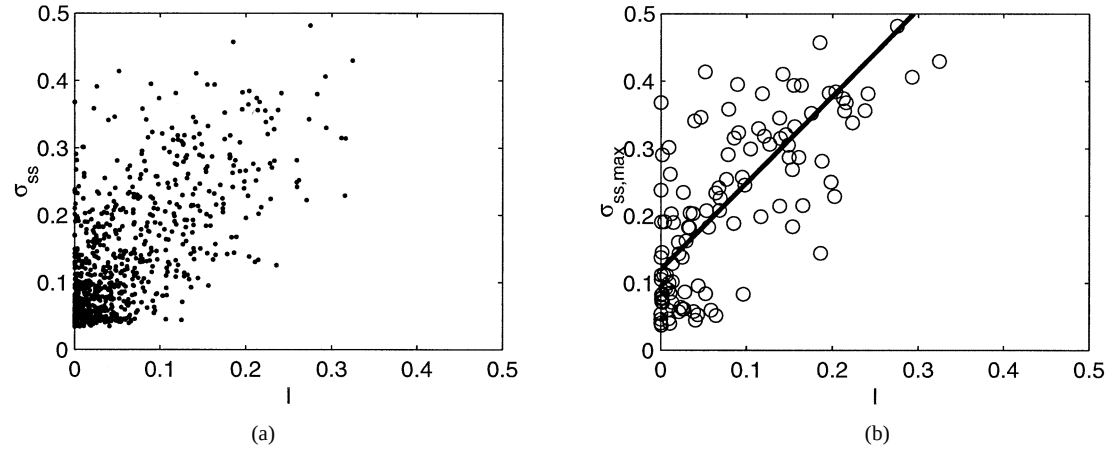

Fig. 13. Instantaneous σ^0_{ss} versus I during (a) sea spike events (slope $= 1.14$, $r^2 = 0.68$) and (b) only at sea spike maxima (slope $= 1.29$, $r^2 = 72$), using all video data at 46° grazing.

with the simultaneous I values. The linear fit to these data gives $\sigma^0_b = 0.71$ (-1.5 dB), but we note that this is only a subset of the available data.

Fig. 12(a) compares the instantaneous values of σ^0_{ss} and I for the sea spike events in all five records at 31° grazing. The beam-filling factors were determined using the intensity thresholds of maximum correlation. The data show an increased scatter but there still appears to be a linear relationship. Again, looking only at the values at the sea spike maxima limits the effects of the trailing foam. Fig. 12(b) compares the data at the sea spike maxima and the linear fit yields $\sigma^0_b = 0.64$ (-1.9 dB). The standard deviation of the slope based on estimates from individual records is 0.05, which suggests that σ^0_b is bounded by -2.3 and -1.6 dB.

A similar analysis was performed on the 46^0 data as shown in Fig. 13. There is a significant increase in the scatter for the higher grazing angle data and the correlation between NRCS and beam-filling is significantly smaller than for the 31° data. The subset of data from the spike maxima suggests that a linear relationship may exist with an increase in the slope to a value of 1.29. This increase in slope implies an increase in the NRCS of breaking regions at higher grazing angles to range of 0.12 dB $< \sigma^0_b <$ 1.9 dB. However, it is our opinion that a definitive conclusion can not be drawn from these higher grazing angle data due to the significant differences in the wave field that existed close to the pier. These wave field differences not only lead to more complicated wave breaking effects, but also had a negative impact on our ability to systematically define wave breaking in the video records. Therefore, no further analyses can be performed on the higher grazing angle data, and we show it here for completeness only.

IV. Summary

Presented herein are measurements of radar backscatter from an X-band scatterometer along with simultaneous video recordings made at a field beach during low-amplitude swell wave conditions and mild winds. For the first time, the radar and video signals from shallow water breaking waves are compared quantitatively. In general, the data show that breaking events generate large amplitude returns in both sensors and, based on subjective visual observation, the radar sea spikes show a higher correlation ($\sim 92\%$) with breaking events than has been observed in similar studies of deepwater wave breaking. In addition, the radar backscatter from shallow water breaking events is shown to contribute up to 40% to 50% of the total cross section for these data, which is a much larger contribution than previously observed for deepwater breaking events. This highlights the increased importance of understanding how wave breaking influences radar backscatter in nearshore areas.

Using simultaneous (digitized) video recordings of the water surface illuminated by the radar, the horizontal size of individual breaking events was estimated based on a threshold gray scale intensity value. Variations in the ambient light conditions and viewing geometries were accounted for through a correlation analysis, and the estimated breaking areas were converted to a normalized "beam-filling factor" in order to make a direct comparison with the radar measurements. The results show that, when the appropriate video gray scale threshold is chosen, the beam-filling factor calculated from the video is well correlated with the instantaneous cross section during a radar sea spike. This supports the hypothesis that the primary scattering from breaking waves is due to the highly roughened water generated by turbulence at the wave crest. This is in contrast to the specular scattering mechanism suggested by previous field studies of deepwater breakers, although we cannot rule out the possibility that specular scattering may contribute more significantly at the initial stages of breaking, especially when looking directly upwave.

The present data indicate that for a grazing angle of 31° the NRCS from active breaking regions (σ_b^0) can be approximated by a spatially constant value of approximately -1.9 dB. This value compares favorably with the value of -3 dB given in [28] for upwave looks (vertical–vertical polarization) and stationary deepwater breakers in the laboratory. It should be noted that shallow water breaking waves are often similar to turbulent bores, which propagate long distances with little change in shape, and are frequently modeled as such. This is the likely reason why these field measurements of breaking wave NRCS are similar to the lab measurements of stationary breakers. Also, on the day of the field experiment, winds were very light and the highly transient wind-induced spilling breaking that is commonly observed in deep water did not occur in the observation area.

Perhaps more important than the numerical value of σ_b^0 is the finding that σ_b^0 can be well approximated by a spatially constant value, this result has several ramifications. First, this implies that variations in sea spike amplitudes are strictly dependent on the amount of beam-filling that occurs. Therefore, the net contribution of breaking events to the total cross section is a function of both the frequency of breaking and the relationship between the radar footprint area and the scale of the breaking waves. We suggest that associating the sea spike cross section with the size of the breakers is an important step in removing any ambiguities in the interpretation of sea spike measurements.

Furthermore, since the horizontal extent of the active breaking area is proportional to the measured NRCS, an imaging radar system with a large viewing area (and reasonably fine resolution) could be used to measure the occurrence and spatial extent of wave breaking in the surf zone. Video systems are already being utilized for this purpose, however, the present results also highlight certain advantages for using radar over video remote sensing. In particular, radar is less responsive to relict foam not directly associated with wave breaking and requires less "tuning" to differentiate between breaking and nonbreaking. This becomes of particular importance when analyzing wave breaking on a wave-by-wave basis; such measurements are difficult if not impossible to make with *in situ* senors over a large areas. On the other hand, if only the mean location of wave breaking is of interest then time-exposure techniques work quite well in removing the influence of relict foam from video-based wave breaking measurements.

Finally, these results suggest that X-band radar can be a useful tool for studying surf zone wave breaking processes, and these results will also be of use in the development of radar scattering models for nearshore areas where shallow water breaking is common. The biggest drawback of the present results is that the question of the variation of σ_b^0 with grazing angle is left unanswered. This is an unfortunate consequence of less than ideal experimental conditions. Learning more about the variation of σ_b^0 with grazing angle and ambient wind conditions is a priority for future surf zone radar applications.

ACKNOWLEDGMENT

The authors would like to acknowledge D. Kletzli (Veridian Systems) for construction of the radar system and Z. Williams (Arete Associates) for the use of video equipment during the experiment. We would also like to thank the staff at the FRF for their gracious assistance and C. Wackerman (Veridian Systems) for several helpful discussions about this work.

REFERENCES

[1] A. J. Bowen, "The generation of longshore currents on a plane beach," *J. Mar. Res.*, vol. 27, pp. 206–215, 1969.
[2] T. C. Lippmann, R. A. Holman, and A. J. Bowen, "Generation of edge waves in shallow water," *J. Geophys. Res.*, vol. 102, pp. 8663–8679, 1997.
[3] I. A. Svendsen, "Analysis of surf zone turbulence," *J. Geophys. Res.*, vol. 92, pp. 5115–5124, 1987.
[4] T. C. Lippmann and R. A. Holman, "Quantification of sand bar morphology: A video technique based on wave dissipation," *J. Geophys. Res.*, vol. 94, pp. 995–1011, 1989.
[5] C.-A. Zimmermann and R. Seymour, "Detection of breaking in a deep water wave record," *J. Waterway, Port, Coastal Ocean Eng.*, vol. 128, no. 2, pp. 72–78, 2002.
[6] J. R. Gemmrich and D. M. Farmer, "Observations of the scale and occurrence of breaking surface waves," *J. Phys. Oceanogr.*, vol. 29, pp. 2595–2606, 1999.
[7] E. C. Monahan, "Oceanic whitecaps," *J. Phys. Oceanogr.*, vol. 1, pp. 139–144, 1971.
[8] H. F. Stockdon and R. A. Holman, "Estimation of wave phase speed and nearshore bathymetry from video imagery," *J. Geophys. Res.*, vol. 105, pp. 22 015–22 033, 2000.
[9] A. T. Jessup, C. J. Zappa, M. R. Loewen, and V. Hesany, "Infrared remote sensing of breaking waves," *Nature*, vol. 385, pp. 52–55, 1997.
[10] L. Ding and D. M. Farmer, "Observations of breaking surface wave statistics," *J. Phys. Oceanogr.*, vol. 24, pp. 1368–1387, 1994.
[11] M. Katzin, "On the mechanism of radar sea clutter," *Proc. IRE*, vol. 45, pp. 44–54, 1957.
[12] M. W. Long, "On the two-scatterer theory of sea echo," *IEEE Trans. Antennas Propagat.*, vol. AP-22, pp. 667–672, 1974.
[13] D. R. Lyzenga and R. A. Shuchman, "Analysis of scatterer motion effects in MARSEN *X* band SAR imagery," *J. Geophys. Res.*, vol. 88, pp. 9769–9775, 1983.
[14] A. T. Jessup, W. K. Melville, and W. C. Keller, "Breaking waves affecting microwave backscatter 1, detection and verification," *J. Geophys. Res.*, vol. 96, pp. 20 547–20 559, 1991.
[15] Y. Liu, S. J. Frasier, and R. E. McIntosh, "Measurement and classification of low-grazing-angle radar sea spikes," *IEEE Trans. Antennas Propagat.*, vol. 46, pp. 27–40, Jan. 1998.
[16] S. J. Frasier, Y. Liu, and R. E. McIntosh, "Space-time properties of radar sea spikes and their relation to wind and wave conditions," *J. Geophys. Res.*, vol. 103, pp. 18 745–18 757, 1998.

[17] S. J. Frasier, Y. Liu, D. Moller, and R. E. McIntosh, "Directional ocean wave measurements in a coastal setting using a focused array imaging radar," *IEEE Trans. Geosci. Remote Sensing*, vol. 33, pp. 428–440, Mar. 1995.
[18] P. S. Bell, "Shallow water bathymetry derived from an analysis of X-band marine radar images of waves," *Coastal Eng.*, vol. 37, pp. 513–527, 1999.
[19] D. B. Trizna, "Errors in bathymetric retrievals using linear dispersion in 3-D FFT analysis of marine radar ocean imagery," *IEEE Trans. Geosci. Remote Sensing*, vol. 39, pp. 2465–2469, Nov. 2001.
[20] J. A. McGregor, E. M. Poulter, and M. J. Smith, "*S* band Doppler radar measurements of bathymetry, wave energy fluxes, and dissipation across an offshore bar," *J. Geophys. Res.*, vol. 103, pp. 18 779–18 789, 1998.
[21] B. L. Lewis and I. D. Olin, "Experimental study and theoretical model of high-resolution radar backscatter from the sea," *Radio Sci.*, vol. 15, pp. 815–828, 1980.
[22] P. H. Y. Lee, J. D. Barter, K. L. Beach, C. L. Hindman, B. M. Lake, H. Rungaldier, J. C. Shelton, A. B. Williams, R. Yee, and H. C. Yuen, "X band microwave backscattering from ocean waves," *J. Geophys. Res.*, vol. 100, pp. 2591–2611, 1995.
[23] D. S. W. Kwoh and B. M. Lake, "A deterministic, coherent, and dual-polarized laboratory study of microwave scattering from water waves, 1, short gravity waves without wind," *IEEE J. Oceanic Eng.*, vol. OE-9, pp. 291–308, 1984.
[24] A. I. Kalmykov and V. V. Pustovoytenko, "On the polarization features of radio signal scattered from the sea surface at small grazing angles," *J. Geophys. Res.*, vol. 81, pp. 1960–1964, 1976.
[25] D. R. Lyzenga, A. L. Maffett, and R. A. Shuchman, "The contribution of wedge scattering to the radar cross section of the ocean surface," *IEEE Trans. Geosci. Remote Sensing*, vol. GE-21, pp. 502–505, 1983.
[26] D. R. Lyzenga and E. A. Ericson, "Numerical calculations of radar scattering from sharply peaked ocean waves," *IEEE Trans. Geosci. Remote Sensing*, vol. 36, pp. 636–646, Mar. 1998.
[27] M. L. Banner and E. H. Fooks, "On the microwave reflectivity of small-scale breaking water waves," in *Proc. R. Soc. London A*, vol. 399, 1985, pp. 93–109.
[28] D. T. Walker, D. R. Lyzenga, E. A. Ericson, and D. E. Lund, "Radar backscatter and surface roughness measurements for stationary breaking waves," in *Proc. R. Soc. London A*, vol. 452, 1996, pp. 1953–1984.
[29] O. M. Phillips, "Radar returns from the sea surface-Bragg scattering and breaking waves," *J. Phys. Oceanogr.*, vol. 18, pp. 1065–1074, 1988.
[30] A. T. Jessup, W. C. Keller, and W. K. Melville, "Measurements of sea spikes in microwave backscatter at moderate incidence," *J. Geophys. Res.*, vol. 95, pp. 9 679–9688, 1990.
[31] A. T. Jessup, W. K. Melville, and W. C. Keller, "Breaking waves affecting microwave backscatter 2, dependence on wind and wave conditions," *J. Geophys. Res.*, vol. 96, pp. 20 561–20 569, 1991.

Merrick C. Haller received the B.S. degree from Purdue University, West Lafayette, IN, in 1993, and he received the M.C.E. and Ph.D. degrees in coastal engineering from the University of Delaware, Newark, in 1996 and 1999, respectively.

He is currently an Assistant Professor in the Department of Civil, Construction, and Environmental Engineering, with a joint appointment in the College of Oceanic and Atmospheric Sciences, both at Oregon State University, Corvallis. He has held a joint research appointment at the Environmental Research Institute of Michigan, Ann Arbor, and the University of Michigan, Ann Arbor, from 1999 to 2001. His present research interests include remote sensing of the nearshore ocean, wave breaking, rip currents, and coastal modeling.

David R. Lyzenga received simultaneous B.S. degrees from Calvin College, Grand Rapids, MI, and the University of Michigan, Ann Arbor, in 1967, the M.S. degree in physics from Yale University, New Haven, CT, in 1968, and the Ph.D. degree in electrical engineering from the University of Michigan, in 1973.

He currently holds joint research appointments at Veridian Systems Division, Ann Arbor, and the University of Michigan. He has worked at the Environmental Research Institute of Michigan, Ann Arbor, from 1974 to 1987, and was an Associate Professor in the College of Marine Studies, University of Delaware, Newark, from 1987 to 1989. His research interests include surface wave dynamics, interactions of electromagnetic radiation with the ocean, and remote sensing of the ocean using both radar and optical techniques.